Bioactive Materials 25 (2023) 86–94

Contents lists available at ScienceDirect

Bioactive Materials

journal homepage: www.keaipublishing.com/en/journals/bioactive-materials

Radiofrequency induced heating of biodegradable orthopaedic screw implants during magnetic resonance imaging

Jonathan Espiritu [a,*], Mostafa Berangi [b,c,d], Hanna Cwieka [e], Kamila Iskhakova [e], Andre Kuehne [b], D.C. Florian Wieland [e], Berit Zeller-Plumhoff [e], Thoralf Niendorf [b,c,d], Regine Willumeit-Römer [e], Jan-Marten Seitz [a]

[a] Syntellix AG, Hannover, Germany
[b] MRI.TOOLS GmbH, Berlin, Germany
[c] Charité – Universitätsmedizin Berlin, Corporate Member of Freie Universität Berlin and Humboldt Universität zu Berlin, Berlin, Germany
[d] Berlin Ultrahigh Field Facility (B.U.F.F.), Max-Delbrueck Center for Molecular Medicine in the Helmholtz Association, Berlin, Germany
[e] Institute of Metallic Biomaterials, Helmholtz Zentrum Hereon, Geesthacht, Germany

ARTICLE INFO

Keywords:
Biodegradable implants
Magnesium
Medical imaging
Magnetic resonance imaging
Patient safety

ABSTRACT

Magnesium (Mg)-based implants have re-emerged in orthopaedic surgery as an alternative to permanent implants. Literature reveals little information on how the degradation of biodegradable implants may introduce safety implications for patient follow-up using medical imaging. Magnetic resonance imaging (MRI) benefits post-surgery monitoring of bone healing and implantation sites. Previous studies demonstrated radiofrequency (RF) heating of permanent implants caused by electromagnetic fields used in MRI. Our investigation is the first to report the effect of the degradation layer on RF-induced heating of biodegradable orthopaedic implants.

WE43 orthopaedic compression screws underwent *in vitro* degradation. Imaging techniques were applied to assess the corrosion process and the material composition of the degraded screws. Temperature measurements were performed to quantify implant heating with respect to the degradation layer. For comparison, a commercial titanium implant screw was used.

Strongest RF induced heating was observed for non-degraded WE43 screw samples. Implant heating had shown to decrease with the formation of the degradation layer. No statistical differences were observed for heating of the non-degraded WE43 material and the titanium equivalent. The highest risk of implant RF heating is most pronounced for Mg-based screws prior to degradation. Amendment to industry standards for MRI safety assessment is warranted to include biodegradable materials.

1. Introduction

Rise in aging population, technological advancements, and availability of better medical facilities drive the prevalence of orthopaedic implantations [1]. With the resorption of biodegradable materials, the need for implant removal using secondary surgery is averted along with significant reduction of patient burden and health care costs. Interest in magnesium (Mg)-based materials has shown exponential increase as a contemporary alternative to traditional permanent implants [2–5]. The appeal is warranted by the material's appropriate biocompatibility [6] and mechanical properties [3].

Postoperative care of orthopaedic implants is aided by imaging of implantation sites to monitor the healing process of surrounding bone and tissues, and to assess the implant status [7–9]. MRI presents a viable approach for the examination of implantation sites due to its superb bone-soft tissue contrast and the use of non-ionizing radiation. Mg-based implants have shown to be compatible with MRI providing good visualization due to their lower metallic artefact production [9]. However, the metallic and electrically conductive nature of Mg-based and other metallic implants constitutes challenges for MRI. Implant and tissue heating due to interactions between conductive implants and electromagnetic (EM) fields may lead to tissue heating and thus compromise patient safety [10].

Implant heating may be induced by exposure to two time-varying

Peer review under responsibility of KeAi Communications Co., Ltd.
* Corresponding author.
E-mail address: espiritu@syntellix.com (J. Espiritu).

https://doi.org/10.1016/j.bioactmat.2023.01.017
Received 23 November 2022; Received in revised form 19 January 2023; Accepted 21 January 2023
Available online 23 January 2023

fields required for MRI: RF field transmission (B_1^+) induced heating and heating caused by switched magnetic field gradients (B_G) [10]. MRI uses radiofrequency (RF) power transmission for signal and image generation. Having base frequencies in the MHz, B_1^+ is provided by a transmit RF coil used for spin excitation. Spatial encoding used for MR image generation is achieved by switched magnetic field gradients B_G, with frequencies found in the kHz range [11,12]. Following Faraday's law, time-varying magnetic fields are inherently accompanied by electric fields (E-fields), generating so called eddy currents. Induced eddy currents can deposit power into implants and further induce secondary EM fields around the implant, which may cause tissue heating. Owing to the material, shape, location, orientation, and degradation state of a conductive implant, the level of RF power deposition induced heating and heating induced by switched magnetic field gradients may vary [13,14].

Due to the geometry of orthopaedic screws, RF heating is of critical concern. The specific absorption rate (SAR) describes the temporal averaged absorbed RF power P_{RF} over time per exposed mass Δm [10]:

$$SAR = \frac{\langle P_{RF} \rangle_t}{\Delta m} = \frac{\sigma \langle |E|^2 \rangle_t}{2\rho}$$

As such, the SAR is governed by tissue parameters and MRI hardware. Electrical conductivity σ and mass density ρ are inherent to the surrounding tissue, while the E-field E is dictated by the imaging hardware. To limit heating and to prevent high SAR, MR techniques and protocols have been modified by reducing the power of RF excitation pulses and by increasing the repetition time between RF excitation pulses. A plethora of reports presents more sophisticated MRI hardware and methodology tailored for mitigation of RF induced implant heating [15–17]. Pioneering approaches include modification of RF transmission fields using RF arrays and parallel transmission with maximum and null current modes [18,19].

The induced eddy currents caused by the effective transmission field B_1^+ are condensed to the surface of the metal due to the "skin effect", a law of electrodynamics. Though the heating of the small implant mass (such as a screw) may be negligible, the secondary (scattered) E-field induced by the eddy currents becomes hazardous at critical locations along the implant [10]. RF currents indirectly induced in the neighbouring tissue by the secondary E-field are thus the major contributor to RF induced heating. Furthermore, thin wires, screws, and other one-dimensional-like geometries may succumb to the "antenna effect". This effect describes intensity peaks when the implant length falls within one-quarter to one-half of the RF wavelength found in tissue [20]. Thus, elevated heating may be observed for thin geometries since the secondary E-field is optimal under these conditions, more predominantly at the implant tip ends.

Prior to market entry, various tests are undertaken to ensure medical devices conform to their respective standards. With support from governmental agencies, international standards have been established to ensure patient safety during MRI studies [10]. Noteworthy standards regarding implant heating in MRI include ASTM F2182 [21], IEC 60601-2-33 [22], and ISO/TS 10974 [23]. To this end, responsibility falls upon manufacturers of medical devices to minimize hazardous risk and uphold patient safety.

Previous studies have documented heating caused by permanent metallic implants in MRI [11,24–26]. Furthermore, particular studies have utilised computational modelling methods to estimate RF-induced heating [27–30]. Mg-based materials have additionally been employed for thermal ablation of tumours utilising the eddy thermal effect [31]. However, the literature does not reveal reports elucidating RF induced heating of biodegradable orthopaedic implants. How the degradation layer can affect potential heating in MRI is of high clinical relevance, still unknown and warrants additional exploration. To close this gap, this study first carefully characterizes the degradation layer of *in vitro* corroded Mg-based biodegradable orthopaedic compression screws (WE43) using micro computed tomography, X-ray diffraction, scanning electron microscopy and energy dispersive X-Ray electron microscopy. This material characterization is followed by an examination of the impact of the degradation layer state on RF-induced heating in MRI of WE43 materials. For evaluation, temperature profiles obtained for WE43 material are benchmarked against temperature profiles derived from a commercial titanium implant screw equivalent. We hypothesise that the degradation layer formed around the base material of a Mg-based biodegradable screw over time disrupts secondary E-field distribution which may lessen RF heating of the surrounding environment, and may benefit MRI aided monitoring of implantation sites.

2. Materials and methods

2.1. Sample preparation

Mg-based (WE43) orthopaedic compression screws (Syntellix AG, Hannover, Germany) 40 mm in length and 3.2 mm in diameter underwent *in vitro* degradation. The WE43 alloy is comprised of magnesium alloyed with Yttrium, Rare Earth Elements, and Zirconium [32]. To compare the heating profile of a non-degraded WE43 sample to alternatives, a titanium commercial equivalent was included (Fig. 1). The WE43 samples were immersed and corroded in a modified ASTM F3268 Standard [33] with Dulbecco's Phosphate Buffered Saline (DPBS). As described by the standard, the temperature of the corrosion medium was kept at 37 ± 1 °C with a pH of approximately 7.4 ± 0.2. A specimen was placed in 2.5 L of the medium which was kept constant and replaced if evaporation were to occur. If a measured pH registered above a pH of 7.6, the corrosion medium was treated with a HCl buffering solution.

24 screws were immersed and degraded in the solution for eight time points (three samples per time point) ranging from one-week to eight-weeks with an increment of one week. Once the specified immersion time elapsed, the samples underwent cleaning with distilled water and were rinsed with ethanol to remove salts and prevent further oxidation. The Ti sample was assumed to have negligible degradation within the time frame of this degradation setup.

2.2. Material characterisation

A randomly selected subset of the degraded screws for each time-period was chosen to be imaged with various techniques to provide qualitative and quantitative data of the degradation layer developed under the chosen corrosion method.

2.2.1. Micro-computed tomography

The *in vitro* degraded screws underwent micro-computed tomography (μCT) to observe changes to the geometry of the screw as corrosion time continued. The samples were first imaged by a laboratory μCT scanner (Phoenix Nanotom by Baker Hughes, Celle, Germany) with scanning parameters described in Table 1. The scans were reconstructed in Datos|x (Baker Hughes, Celle, Germany) where potential movement caused by the rotating stage was corrected using an optimisation function. The raw data was then segmented using Fiji/ImageJ [34] by first applying anisotropic diffusion to reduce noise. Then, a trainable WEKA segmentation [35] was applied to segment the base material, degradation layer, and background. Additionally, the segmented base material was utilised to calculate the mass loss of the degraded samples.

2.2.2. X-ray diffraction

X-ray diffraction (XRD) was performed at P07 side station at the PETRA III storage ring at Deutsches Elektronen-Synchrotron (DESY, Hamburg, DE) [36] to describe the crystalline structure of the degradation layer. An X-ray beam with an energy of 87.1 keV and 0.5 beam size was applied to the top of two-, four-, six-, and eight-week time point screw samples a total of three times each. A Perkin Elmer XRD 1621 Flat Panel Detector (PerkinElmer, Waltham, United States) was placed at

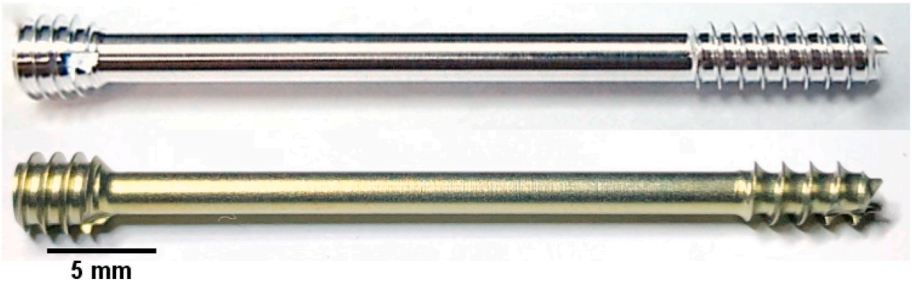

Fig. 1. 40 mm Mg-based orthopaedic compression screw MAGNEZIX® CS ø 3.2 (top) and Ti equivalent (bottom), reproduced under the CC BY-NC-ND 4.0 License [9].

Table 1
μCT measurement parameter details applied to image the degraded WE43 screw samples.

Scanning Parameter	Value
Sample distance [mm]	20
Detector distance [mm]	200
Timing per projection [ms]	2400
Frames per projection	5
Number of images	2000
Voltage [kV]	125
Current [μA]	45
Isotropic voxel size [μm]	5

1.485 m from the samples. The samples were subjected to 0.5 s of exposure time. Lanthanum hexaboride (Lab6) was used as a calibrant. The acquired XRD images were processed using Dawn Science 2.18.0 (Diamond Light Source, Didcot, UK) [37]. Diffractograms were analysed using MATLAB R2018 (The MathWorks Inc., US) and averaged along with a slice in a direction perpendicular to the screw axis. The final plots were normalized according to Mg (101) peak intensity.

2.2.3. Scanning electron microscopy and energy dispersive X-ray spectroscopy

Scanning electron microscopy (SEM) and energy dispersive X-ray spectroscopy (EDX) analysis were employed to characterise the cross section along the longitudinal axis of the degraded screws in terms of qualitative imaging and elemental composition of the degradation layer. Imaging was acquired by a Tescan Vega SB-U III (Tescan, Czech Republic) at Helmholtz-Zentrum Hereon (Geesthacht, Germany). Images were taken in backscattered electron mode (BSE mode) to emphasize the differences between the residual material and the degradation layer. The EDX measurements were performed as mapping of a chosen region of interest. The SEM and EDX measurements details can be found in Table 2. Zero-, Two-, four-, six-, eight-week degraded samples were embedded in methyl methacrylate liquid and powder (Demotec®, Demotec, Germany) before being ground and polished on a Saphir 320/Rubin 520 machine (QATM, Advanced Materialography, Germany). Subsequently, the samples were sputtered with carbon to provide appropriate conductivity for the SEM and EDX measurements.

2.3. Temperature measurements during MRI examination

A 3.0 T (Skyra Fit, Siemens, Erlangen, Germany) MRI scanner was used for *in vitro* measurements. The various degraded samples and titanium equivalent underwent a procedure adapted from ASTM F2182 [21]. The MR scanning parameters used during the heating measurements are summarized in Table 3.

A rectangular case with dimensions defined by the ASTM Standard was constructed from acrylic glass and was filled with a phantom gel. The tissue-mimicking phantom was prepared with 1.32 g/L of NaCl (Sigma Aldrich, Taufkirchen, Germany), 10 g/L of polyacrylic acid (Sigma Aldrich, Taufkirchen, Germany), and 25 L of distilled water. Prior to each specimen heating test, local incident field calibration was performed as described by ASTM F2182 [21].

A non-conducting 3D-printed holder was developed to hold the specimen and to guide fibre-optic probes from the thermometry system (model T1; Neoptix Inc., Québec, Canada) to the tips of the implants which define the highest heating points [38]. A total of three probes were used, two placed at the implant ends, and one control probe placed on the opposite side of the phantom to measure heating sans implant influence. The position of the probes was adjusted between every sample scan to ensure the distance between the probes and the implant was consistent. The holder with a single screw sample was placed centred 2 cm from the phantom wall and aligned to the main magnetic field, as this position has been previously determined as the location with maximum heating [39]. The acrylic case was then placed in a Styrofoam insulation container for scanning as illustrated in Fig. 2.

Prior to heating measurements, the gel phantom was brought to scanning room temperature 24 h beforehand. The temperature was recorded 2 min before and 2 min after the scanning sequence was applied at intervals of 1 s. For each sample, one measurement was taken without the sample, and another measurement was taken with the sample placed in the phantom to assess the increase in temperature due to the device itself. Screw samples from weeks six to eight did not

Table 2
SEM and EDX measurement parameter details applied to image the degraded WE43 screw samples.

Parameter	SEM	EDX
Voltage [kV]	15	15
Magnification [x]	50	2000
Beam intensity [–]	10	15

Table 3
MRI scanning parameters used during heating measurements of the screw samples.

B0 Field strength [T]	3.0
RF coil type (transmission)	Body RF coil
RF coil type (reception)	32 channel spine RF array
Imaging technique	Turbo-spin-echo (TSE)
TR [ms]	5820
Inter-echo time TE [ms]	6.8
Echo train length	8
Imaging Plane	Transversal
Excitation flip angle [°]	120
Pulse Width [ms]	1.28
Transmitter Power [W]	90.7
FOV [mm]	450
Matrix size [pixel]	512
Slice thickness [mm]	3.4
Total slices	24
Whole body-SAR [W/kg]	2
Patient Body Weight [kg]	70
Number of Averages	20
Scan time [s]	939

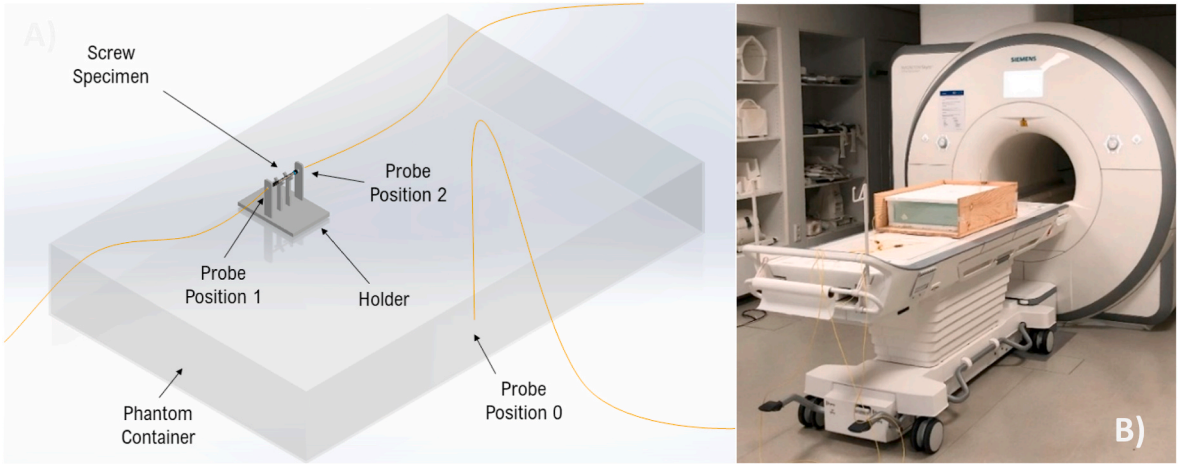

Fig. 2. Heating measurement setup based on ASTM F2182 depicting the MRI scanner (A) and the phantom (B). For the temperature measurements the phantom setup was moved into the isocenter of the MR scanner.

succumb to heating measurements as the samples fractured during the *in vitro* degradation process.

2.4. Statistics

Statistical analyses were performed using RStudio (RStudio, USA). A p-value of <0.05 was chosen to be statistically significant. To compare the increases in temperature and mass loss between the various degraded WE43 time-points, a two-way analysis of variance (ANOVA) was performed. Additionally, the ANOVA test was also applied to determine the differences between the WE43 material and the equivalent titanium implant. If any significant results were determined, a Turkey's post hoc comparison procedure was utilised to perform pairwise comparisons.

3. Results

3.1. Material characterisation

3.1.1. Micro-computed tomography

The degraded specimens were scanned via μCT to capture the physical geometry of both the base material and the degradation products. Time-points after the fifth week were excluded due to specimen breaking during corrosion process. An example is outlined in Fig. 3. Non-uniform pitting corrosion is clearly visible from the μCT images (Fig. 3A). Segmentation applied to the μCT images (Fig. 3B) successfully differentiated base material from the degradation products. From the segmented images, it is evident that the degradation layer unevenly penetrates the base material from the inner canulation and more evidently from the outer surface of the screws. A build-up of degradation product is also visible in the cannulation. A fully realised 3D object file of the base material is visible in Fig. 3C.

The segmented base material was utilised to calculate any significant differences between the mass loss during the selected degradation periods. The statistical tests revealed a significant difference between the degraded timepoints ($p < 0.05$). A summary of the pairwise comparisons are shown in Table 4.

3.1.2. X-ray diffraction

$Mg(OH)_2$, MgO, $MgCO_3$, $CaCO_3$, and $MgHCO_3{\cdot}3H_2O$ degradation products were identified by means of XRD as shown in Fig. 4 (left). The more predominant peaks observed were contributed by $Mg(OH)_2$ and MgO, suggesting the presence of higher crystalline phases of these products. With respect to the time course, the intensity of the $Mg(OH)_2$

Table 4
Post hoc significant differences of paired degradation time points (tp).

Pairwise comparison of degraded tps	p-value
1tp:0tp	<0.05
2tp:0tp	<0.05
3tp:0tp	<0.05
4tp:0tp	<0.05
5tp:0tp	<0.05
2tp:1tp	0.55
3tp:1tp	<0.05
4tp:1tp	<0.05
5tp:1tp	<0.05
3tp:2tp	0.31
4tp:2tp	<0.05
5tp:2tp	<0.05
4tp:3tp	<0.05
5tp:3tp	<0.05
5tp:4tp	0.99

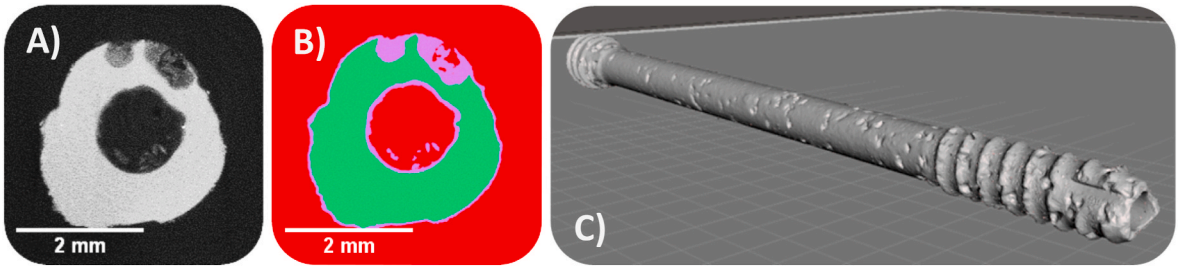

Fig. 3. Exemplary results derived from μCT of degraded specimens. The raw μCT data (A) showing a cross-section approximately 12 mm from the top of the screw is first segmented (B) to create a 3D view (C). The segmented image shows the base metallic material in green, degradation product in purple, and background pixels in red.

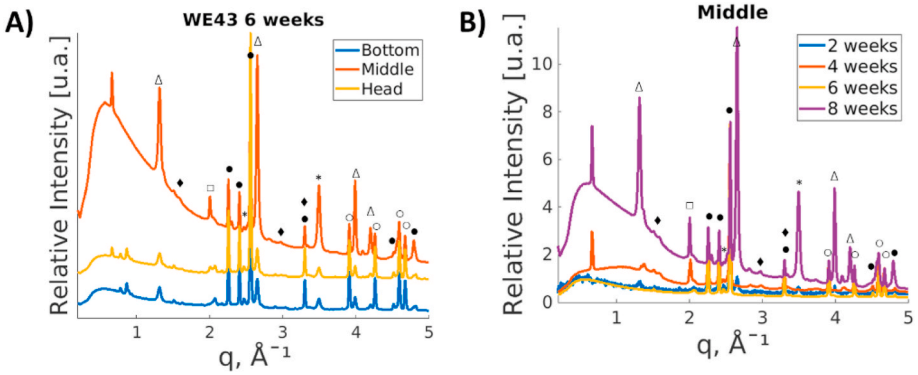

Fig. 4. Diffractograms for the middle section of the screws after two, four, six, and eight weeks in solution (A). Peak assignment is illustrated with the following symbols: ● for Mg, Δ for $Mg(OH)_2$, ○ for MgO, * for $MgCO_3$, ◊ for CaCO3, and □ for $MgHCO_3{\cdot}3H_2O$. Diffractograms of the head, middle, and bottom parts of three averaged samples after eight weeks of immersion time (B). The intensities are normalized with respect to (101) Mg Bragg's peak.

peaks increased with degradation period, while MgO remained at a constant intensity. Additionally, Fig. 4 (right) shows the averaged diffractograms from different locations along the screw. The head, middle, and bottom of the 8-week corroded samples were selected for analysis due to large presence of degradation products. The differences in diffractograms taken at the head and bottom of the screw are negligible. However, there is a significant increase of $Mg(OH)_2$ peaks in the middle section where most degradation products settled within the cannulation. Moreover, most of the diffractograms demonstrated a strong amorphous signal with a peak at 0.55 $Å^{-1}$. Other identified degradation products ($MgCO_3$, $CaCO_3$, $MgHCO_3{\cdot}3H_2O$) did not show significant changes in intensity with time.

3.1.3. Scanning electron microscopy and energy dispersive X-ray

Fig. 5 shows SEM images captured with 50x magnification of the degraded WE43 screw heads of the cannulated screws over the immersion time. For comparison a non-degraded sample (0 weeks) is used as a reference. Material degradation is clearly visible with the loss of screw threads as immersion time persists. The regular and cracked degradation layer develops in the same fashion in the cannulation of the screw as on the exterior surface. A decrease in surface smoothness is noticeable as corrosion continues.

EDX was applied to identify and determine the distribution of elements throughout the degradation layer. The following elements were detected: Mg, Y, Nd, Zr, Na, Cl, K, P, O, and Ca. The elemental composition was measured as maps and is plotted as graphs of weight percentage (Fig. 6). Based on SEM and EDX results, the main composition of the degradation layer at two weeks is made of Mg and O. Y, Zr, and Nd are found to have high concentration near the top of the degradation layer and decreases to expected values near the base material. After four weeks, Mg and O remain the main components of the degradation layer with both contents above 25%. The distribution of the other elements remains constant throughout the whole degradation layer with O significantly decreasing near the base material. Results after six weeks display similar distribution of elements as seen after four weeks. About half of the degradation layer is now comprised of O. The degradation layer is thick with many visible cracks. At eight weeks, the degradation is at the highest and is spread well into the cannulation. The degradation layer consists of mainly Mg and O (25% and 50% respectively) with Mg rapidly growing as a residual material. There are no observations of smooth changes at the interface between the degradation layer and base material of the screw.

3.2. Heating measurements during MRI examination

Results derived from the heating measurements are summarized in Fig. 7. As corrosion time increased, a decline in maximum temperature change ΔT was observed, however, there was no apparent quantifiable correlation. The highest average temperature increase was seen at 0-weeks corrosion at 100% of the screw volume and the lowest temperature increase was observed at 3-weeks of corrosion time. The maximum RF-induced heating was measured to be $\Delta T = 1.20 \pm 0.29$ °C for the non-degraded WE43 screw and $\Delta T = 1.16 \pm 0.18$ °C for the titanium equivalent. However, no significant differences were observed.

4. Discussion

The increasing number of orthopaedic implantations continues to drive the need for post-surgery imaging to monitor bone healing and implant placement. MRI of implantation sites provides excellent bone-tissue contrast that may aid postoperative care of orthopaedic implants. Careful risk assessment of RF induced heating of conducting implants is mandatory before MRI can be applied for monitoring of implantation sites. Recognizing this need and opportunity, this study adds to the literature by examining the material characteristics, corrosion dynamics, and the influence of the degradation layer on RF-induced heating of Mg-based implants.

Unlike standard titanium and stainless-steel material, Mg-based implants degrade over time when exposed to bodily fluid. As a result, the chemical composition of the implant and physical geometry change as healing occurs. Since material composition and implant form influence the RF-heating of metallic implants, our study used various imaging techniques to characterise *in vitro* corroded WE43 screws. It is noted that the *in vitro* degradation technique employed in this investigation

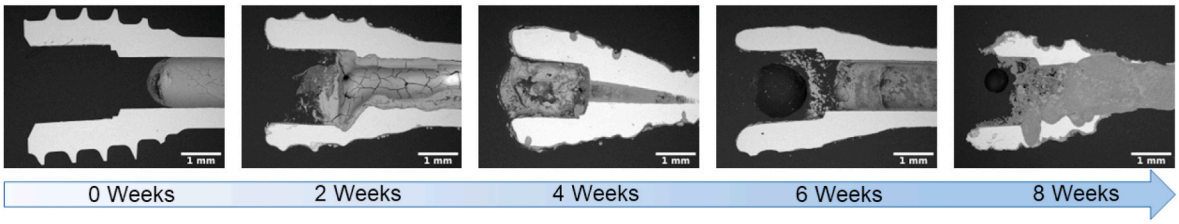

Fig. 5. SEM images of the WE43 screw heads after several time points of *in vitro* immersion.

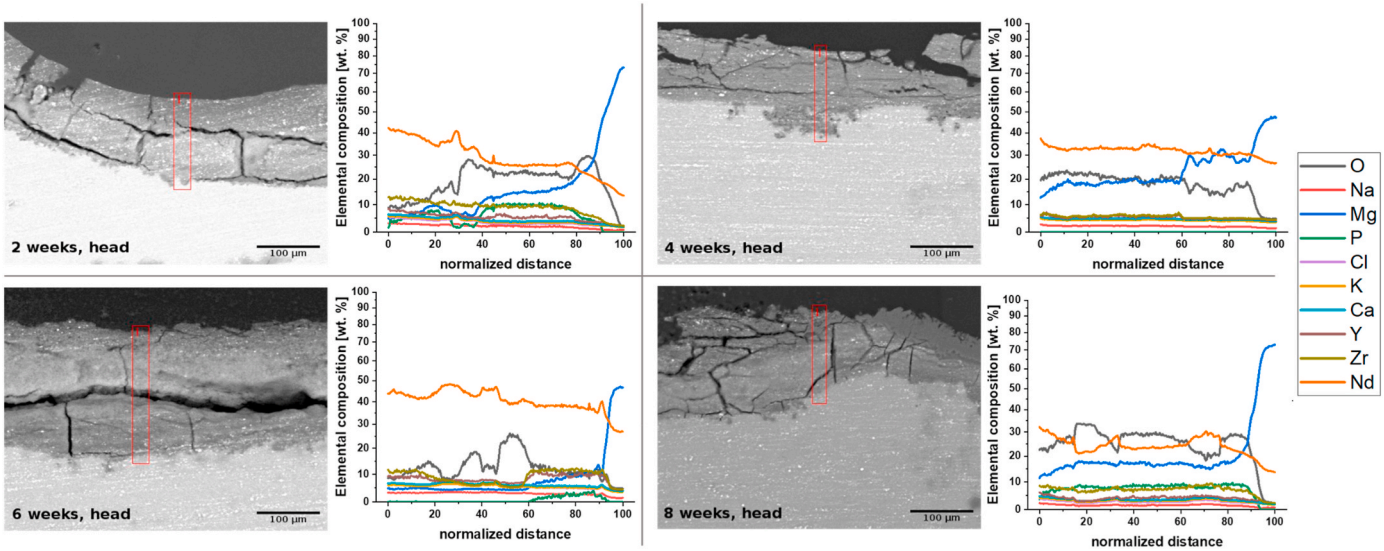

Fig. 6. Regions of interest measured EDX maps and graphs of weight percentage depending on normalized distance where 0 is the sample surface and 100 is the residual metal. Results of samples after 2, 4, 6 and 8 weeks of *in vitro* immersion.

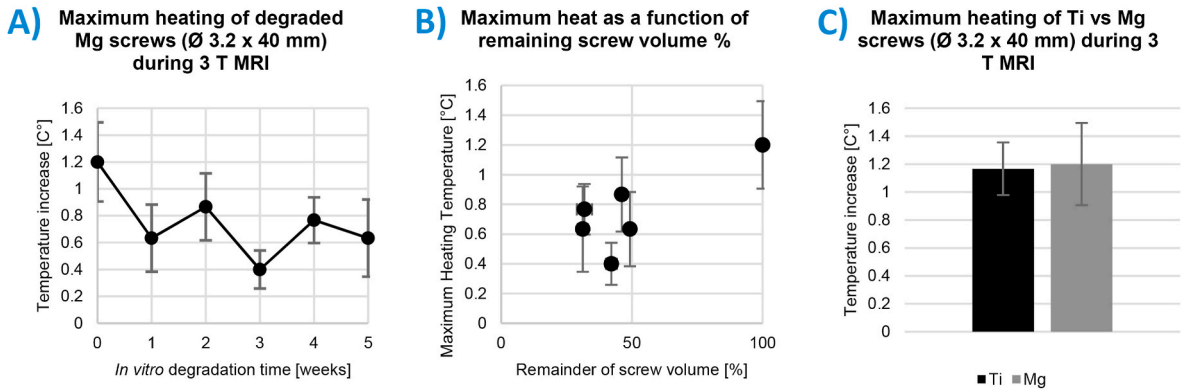

Fig. 7. Maximum RF-induced temperature heating at the tip of the screws of different length. A: influence of corrosion time on heating. B: maximum heating as a function of remainder screw volume. C: Comparison of Mg to commercial Ti equivalent.

provides only a partial impression of the complex processes in which degradation occurs in the human body, because our *in vitro* approach does not factor in the influence of biological material or cell adhesion [40].

The results derived from µCT and SEM provide insight into the physical corrosion of the screw structure *in vitro,* which is supported by previous literature [40]. The segmented µCT images reveal a statistically significant reduction in base metallic WE43 material surrounded by degradation layer as weeks progress. The non-uniformity of degradation is apparent with pit formations of various sizes. SEM images depict surface cracking of the irregular degradation layer. Additionally, the loss of threads is apparent in both µCT and SEM images as the original screw shape begins to lose definition and transforms into a tube-like structure over time. The pitting behaviour seen in Figs. 3 and 5 causes a non-uniform degradation layer and a buildup of degradation product found in the canulation of the screw.

XRD findings identified different crystalline degradation products along various locations of the screw in Fig. 4. The main degradation products were found to be $Mg(OH)_2$ and MgO, which correlates with published papers [41–44]. At eight weeks of degradation, a strong amorphous signal is visible in the middle of the screw, originating from the cannulation which is confirmed by µCT. The presence of this signal suggests the degradation products found in the middle of the screw may possess a non-crystalline amorphous phase, which may be contributed by phosphorus and calcium components [45]. Additionally, a strong Mg $(OH)_2$ signal increases over time and may be the main precipitant in the cannulation of the screw. The lower signals analysed at both ends of the screw suggest a lower presence of degradation material. Thus, the degradation material is mostly composed of $Mg(OH)_2$ in both crystalline and amorphous forms, which is supported by previous works [40].

The EDX analysis revealed high contents of Mg and O as main composition of the degradation layer, confirming degradation products identified in the XRD results. As time persists, O is determined to take further composition of the degradation material. Interestingly, Zr and the rare-earth elements Nd and Y were found to have high concentrations near the surface of the degradation layer, decreasing towards the base material. This "sticking" of rare-earth elements to the surface of the degradation layer is caused by mobility of Yttrium [46]. EDX results suggest compounds consisting of the rare-earth elements are situated near the surface of the samples. Though undetected by XRD in this investigation, previous *in vitro* studies show the identification of Y_2O_3, $Mg_{24}Y_5$, and $Mg_{24}Nd_5$ [47,48].

RF induced heating of conducting implants is influenced by a material's electromagnetic properties and by the physical geometry. Elevated heating is expected at implant lengths half to a quarter of 3.0 T RF wavelengths (13–6.5 cm in tissue) in the body [10], which is not relevant for the 40 mm length implants investigated in this experiment. Since heating is dependent on implant length and main magnetic field

strength, the measured temperatures of the selected 40 mm length screws analysed in this investigation may not be representative for all degradable systems. Moreover, the reported material temperature increases of approximately 1 °C is well under the threshold in which thermal necrosis may occur at 47 °C [49]. Though there were no significant differences between the materials, the non-degraded WE43 implant yielded a minor increase in RF heating over the titanium equivalent (Fig. 7). Winter et al. simulated the secondary E-field distribution of a linear implant while varying the conductivity of the material [10]. The scattered secondary field was found to create hotspots at the implant tips as the conductivity of the material increased. As such, WE43 is reported to have a higher conductivity than titanium [50], which may justify the marginally elevated heating measured. However, Capek et al. have investigated the assumption that current distribution on perfect electric conductors and good conductors (such as copper, aluminum, and silver) are equal [51]. Therefore, similar heating profiles between WE43 materials and titanium are not expected to be significantly different as noted in Fig. 7.

As degradation occurs, not only does the physical geometry of the WE43-based screws change, but the material composition of the implant surface alters as well. As a result, the heating profile of the implant changes as the material corrodes. Our results in Fig. 7 demonstrate that the maximum heating exists at the earliest stage prior to corrosion, more specifically, highest heating at original and largest metallic volume prior to degradation, which is supported by previous work [31]. Although there are no significant differences highlighted, the maximum temperature change found for the degraded implants decreases with degradation time. As corrosion persists two complimentary processes occur, (1) the degradation layer continues to develop as (2) the base metallic material reduces.

The base metallic WE43 material degrades over time transforming the compression screw geometry into a potential one-dimensional or wire-like structure. There is minimal reduction in screw length as the implant degrades. The overall diameter of the base material of WE43 decreases during corrosion. Previous investigations demonstrated that maximum temperature rises caused by RF-heating of thin wires during MRI studies increase as diameter decreases [52]. Armenean et al. describe that the increase in temperature due to the wire diameter reduction is caused by an increased secondary E-field. Subsequently, an increased secondary E-field is developed onto the neighbouring tissue or material. Nonetheless, this finding is not in accordance with the temperature changes observed by our study. This indicates that the developing degradation layer may play a greater influence in the heating profile of Mg-based materials.

As verified by the XRD and EDX results, the $Mg(OH)_2$ layer along with other non-crystalline products continue to develop during degradation and coats the surface of the implant. The physical nature of the degradation layer and its electromagnetic properties influence the heating profile of the corroded screws twofold. First, the induced secondary E-field sensed by the conductive tissue may be dampened by the poorly conductive nature inherent to $Mg(OH)_2$ surrounding the base metallic material. Second, the physical corrosion resulting in a non-smooth surface of the material may disrupt the development of the secondary E-field. Our results demonstrate various sizes of pitting formation and developed surface roughness within the cannulation and on the surface of the screw. The overall surface smoothness is decreased as corrosion persists, which has shown to decrease the “skin effect” of EM fields and therefore reduce current density at the surface of the material [53–55]. Additionally, the secondary E-field may further be hindered by the anisotropic nature of the amorphous degradation material found in the cannulation and the non-uniform sticking of heavier rare-earth metallic elements on the surface of the material. However, the influence of the amorphous material and rare-earth elements on the secondary E-field requires further investigation. As a result, the development of the degradation layer over time may reduce the maximum heating detected by surrounding environment.

The intrinsic degradation capability of Mg-based implants introduces limitations into this investigation. The reactive characteristic of Mg-based alloys prohibits samples from being tested more than once due to the interaction with the water-based phantom medium. As a result, multiple samples must be prepared for each time-point which ultimately differ based on the non-uniform corrosion, which may be the main contributor to the variations in recorded measurements. Additionally, WE43 samples could not be placed in the phantom for extended periods of time, as bubble formation (hydrogen gas) would occur. Although the surrounding area of the temperature probes were verified to be bubble-free prior to measurements, few millimetre-sized bubble formation was seen sparsely formed on the implant due to the corrosion process. This concern justifies an amendment to the ASTM F2182 procedures to include verified and standardised protocols to map RF-induced heating caused by biodegradable materials using MR thermometry [56]. Our investigation focuses on utilising industry *in vitro* standards and testing methodologies as a mandatory precursor to *in vivo* or clinical studies, which would provide further specific information on the impact of the degradation layer on RF induced heating of biodegradable orthopaedic screw implants during MRI. Animal studies would provide further insight on heat dissipation in live tissue and therefor should be investigated in the future. As such, it is important to note that the phantom measurements described by the ASTM standard generally provide an overestimation of the temperature increase due to the lack of blood perfusion, wet tissue convection, and blood vessel conduction effects, all of which would be found *in vivo* and in clinical situations. However, previous studies [57] have shown that although the standard implicitly assumes conservative measurements, the heating responses measured in the ASTM phantom can be greatly underestimated for certain situations which should further caution users of the standardised protocol.

Although RF-induced heating has been investigated for multiple permanent implants, future studies should include heating caused by multiple implants made of biodegradable materials. Additionally, heating profiles of broken Mg-based implants resulting in gaps between the original geometry should be investigated as this may occur *in vivo* [58] which presents further safety risks [10]. Moreover, the effects of degradation products in terms of layer depth and other degradation resultants (hydrogen evolution and pH) should similarly be assessed for influence on implant heating.

5. Conclusion

This is the first study that evaluated RF-induced heating of Mg-based orthopaedic implants during MRI. WE43 screws degraded *in vitro* for various time periods causing decreased RF-induced heating during MRI sessions as corrosion time and the formation of the degradation layer progressed. This reduction in RF-induced heating may be instigated by the decline of the “skin effect” caused by a decrease in surface smoothness during degradation layer formation. To conclude, the non-degraded WE43 sample poses the “worst-case” scenario, suggesting highest heating risk occurs directly after material implantation into the body. RF-induced heating was similar for native WE43 screws and for the titanium equivalent. Though the current ASTM standard was successfully utilised in this investigation, our findings support a revision to industry safety standards to encompass testing of conductive implanted medical devices with verified methodologies which may allow for more optimal evaluations of biodegradable materials.

Conflict of interest

Authors Kuehne and Berangi are employees of MRI.TOOLS GmbH. Author Niendorf is CEO and founder of MRI.TOOLS GmbH. Syntellix AG is a medical technology manufacturer of metallic and bio-absorbable clinical implants. Authors Espiritu and Seitz are employed as Research Associate and Director of Research and Development, respectively.

CRediT authorship contribution statement

Jonathan Espiritu: Conceptualization, Data curation, Formal analysis, Investigation, Methodology, Validation, Visualization, Writing – original draft, Writing – review & editing. **Mostafa Berangi:** Data curation, Formal analysis, Investigation, Methodology. **Hanna Cwieka:** Data curation, Formal analysis, Investigation, Visualization, Writing – original draft. **Kamila Iskhakova:** Data curation, Formal analysis, Investigation, Visualization, Writing – original draft. **Andre Kuehne:** Conceptualization, Methodology, Supervision, Writing – review & editing. **D.C. Florian Wieland:** Data curation, Methodology, Resources, Supervision. **Berit Zeller-Plumhoff:** Data curation, Methodology, Resources, Supervision. **Thoralf Niendorf:** Resources, Supervision, Writing – review & editing. **Regine Willumeit-Römer:** Funding acquisition, Project administration, Resources, Supervision, Writing – review & editing. **Jan-Marten Seitz:** Conceptualization, Funding acquisition, Project administration, Resources, Supervision, Writing – review & editing.

Declaration of Competing interest

Authors Kuehne and Berangi are employees of MRI.TOOLS GmbH. Author Niendorf is CEO and founder of MRI.TOOLS GmbH. Syntellix AG is a medical technology manufacturer of metallic and bio-absorbable clinical implants. Authors Espiritu and Seitz are employed as Research Associate and Director of Research and Development, respectively.

Acknowledgements

We would like to thank Eileen Höltje from Syntellix AG (Hannover, Germany) and Roman Leicht from MRI.TOOLS GmbH (Berlin, Germany) for their assistance with the experiments and preparation of materials. This project has received funding from the European Union's Horizon 2020 Research and Innovation Programme under the Marie Skłodowska-Curie Grant Agreement No 811226.

References

[1] A. Hall, E. Dunstan, Day-case total hip arthroplasty: a safe and sustainable approach to improve satisfaction and productivity, and meet the needs of the orthopaedic population, Orthop. Traumatol. 36 (1) (2022) 14–21.
[2] N. Singh, U. Batra, K. Kumar, N. Ahuja, A. Mahapatro, Progress in bioactive surface coatings on biodegradable Mg alloys: a critical review towards clinical translation, Bioact. Mater. 19 (2023) 717–757.
[3] R.P.S. Krishnan, S. Muthusamy, H. Panchal, M. Alsoufi, A. Ibrahim, A. Elsheikh, Biodegradable magnesium metal matrix composites for biomedical implants: synthesis, mechanical performance, and corrosion behavior -A review, J. Mater. Res. Technol. 20 (2022) 650–670.
[4] Z. Ran, W. Dai, K. Xie, Y. Hao, Advances of Biodegradable Magnesium-Based Implants for," Life Research, vol. 5, 2022, p. 7, 1.
[5] J. Espiritu, M. Meier, J. Seitz, The current performance of biodegradable magnesium-based implants in magnetic resonance imaging: a review, Bioact. Mater. 6 (12) (2021) 4360–4367.
[6] J. Seitz, R. Eifler, F. Bach, H. Maier, Magnesium degradation products: effects on tissue and human metabolism, Jounral of Biomedical Materials Research 102 (10) (2013) 3744–3753.
[7] Z. Mosher, J. Sawyer, D. Kelly, MRI safety with orthopedic implants, Orthopedic Clinics 49 (4) (2018) 455–463.
[8] J. Nzenhuis, S. Park, R. Kamondetdacha, A. Amjad, F. Shellock, A. Rezai, MRI and implanted medical devices: basic interactions with an emphasis on heating, IEEE Trans. Device Mater. Reliab. 5 (3) (2005) 467–480.
[9] J. Espiritu, M. Berangi, C. Yiannakou, E. Silva, R. Francischello, A. Kuehne, T. Niendorf, S. Könneker, R. Willumeit-Romer, J. Seitz, Evaluating metallic artefact of biodegradable magnesium-based implants in magnetic resonance imaging, Bioact. Mater. 15 (2022) 382–391.
[10] L. Winter, F. Seifert, L. Zilberti, M. Murbach, B. Ittermann, MRI-Related heating of implants and devices: a review, J. Magn. Reson. Imag. 53 (6) (2020) 1646–1665.
[11] A. Arduino, U. Zanovello, J. Hand, L. Zilberti, B.R.M. Chiampi, O. Bottauscio, Heating of hip joint implants in MRI: the combined effect of RF and switched-gradient fields, Magn. Reson. Med. 85 (6) (2021) 3447–3462.
[12] R. Brühl, A. Ihlenfeld, B. Ittermann, Gradient heating of bulk metallic implants can be a safety concern in MRI, Magn. Reson. Med. 77 (5) (2017) 1739–1740.
[13] L. Winter, E. Oberacker, C. özerdem, Y. Ji, F. Knobelsdorff-Brenkenhoff, G. Weidemann, B. Ittermann, F. Seifert, T. Niendorf, On the RF heating of coronary stents at 7.0 Tesla MRI, Magn. Reson. Med. 74 (4) (2015) 999–1010.
[14] E. Oberacker, K. Paul, T. Huelnhagen, C. Oezerdem, L. Winter, A. Pohlmann, L. Boehmert, O. Stachs, J. Heufelder, A. Weber, M. Rehak, I. Seibel, T. Niendorf, Magnetic resonance safety and compatibility of tantalum markers used in proton beam therapy for intraocular tumors: a 7.0 Tesla study, Magn. Reson. Med. 78 (4) (2017) 1533–1546.
[15] K. Baker, J. Tkach, J. Nyenhuis, M. Phillips, F. Shellock, J. Gonzalez-Martinez, A. Rezai, Evaluation of specific absorption rate as a dosimeter of MRI-related implant heating, J. Magn. Reson. Imag. 20 (2) (2004) 315–320.
[16] L. Winter, B. Silemek, J. Petzold, H. Pfeiffer, W. Hoffmann, F. Seifert, B. Ittermann, Parallel transmission medical implant safety testbed: real-time mitigation of RF induced tip heating using time-domain E-field sensors, Magn. Reson. Med. 84 (6) (2020) 3468–3484.
[17] Y. Eryaman, E. Turk, C. Oto, O. Algin, E. Atalar, Reduction of the radiofrequency heating of metallic devices using a dual-drive birdcage coil, Magn. Reson. Med. 69 (3) (2012) 845–852.
[18] Y. Eryaman, B. Akin, E. Atalar, Reduction of implant RF heating through modification of transmit coil electric field, Magn. Reson. Med. 65 (5) (2011) 1305–1313.
[19] T. Bachschmidt, M. Köhler, J. Nitsler, C. Geppert, P. Jakob, M. Nittka, Polarized multichannel transmit MRI to reduce shading near metal implants, Magn. Reson. Med. 75 (1) (2016) 217–226.
[20] M. Dempsey, B. Condon, D. Handley, Investigation of the factors responsible for burns during MRI, J. Magn. Reson. Imag. 13 (4) (2001) 627–631.
[21] ASTM International, *ASTM F2182-09 Standard Test Method for Measurement of Radio* Frequency Induced Heating Near Passive Implants during Magnetic Resonance Imaging, 2010. West Conshohocken, PA.
[22] I. E. C. (IEC), EC 60601–2-33:2010+AMD1:2013+AMD2:2015, CSV: Medical Electrical Equipment — Particular Requirements for the Basic Safety and Essential Performance of Magnetic Resonance Equipment for Medical Diagnosis, 2015.
[23] I. O. f. S. (ISO), Assessment of the safety of magnetic resonance imaging for patients with an active implantable medical device, Tech Specif ISOTS (2018), 10974.
[24] R. Buchli, P. Boesiger, D. Meier, Heating effects of metallic implants by MRI examinations, Magn. Reson. Med. 7 (3) (1988) 255–261.
[25] H. Bassen, W. Kainz, G. Mendoza, T. Kellom, MRI-induced heating of selected thin wire metallic implants – laboratory and computational studies – findings and new questions raised, Minim Invasive Ther. Allied Technol. 15 (2) (2006).
[26] S. Tsutsui, T. Matsuda, K. Takeda, M. Sasaki, Y. Kubo, K. Setta, S. Fujiwara, K. Chida, K. Ogasawara, Assessment of heating on titanium alloy cerebral aneurysm clips during 7T MRI, Am. J. Neuroradiol. 43 (7) (2022) 972–977.
[27] Y.C.J. Liu, F. Shellock, W. Kainz, Computational and experimental studies of an orthopedic implant: MRI-related heating at 1.5-T/64-MHz and 3-T/128-MHz, J. Magn. Reson. Imag. 37 (2) (2012) 491–497.
[28] P. Serano, L. Angelone, H. Katnani, E. Eskandar, G. Bonmassar, A novel brain stimulation technology provides compatibility with MRI, Sci. Rep. 5 (9805) (2015).
[29] E. Mattei, M. Triventi, G. Calcagnini, F. Censi, W. Kainz, G. Mendoza, H. Bassen, P. Bartolini, Complexity of MRI induced heating on metallic leads: experimental measurements of 374 configurations, Biomed. Eng. Online 7 (11) (2008).
[30] S. Feng, R. Qiang, W. Kainz, J. Chen, A technique to evaluate MRI-induced electric fields at the ends of practical implanted lead, IEEE Trans. Microw. Theor. Tech. 63 (1) (2014) 305–313.
[31] N. Yang, F. Gong, L. Cheng, H. Lei, W. Li, Z. Sun, C. Ni, Z. Wang, Z. Liu, Biodegradable magnesium alloy with eddy thermal effect for effective and accurate magnetic hyperthermia ablation of tumors, Natl. Sci. Rev. 8 (1) (2021).
[32] AZO Materials, Magnesium elektron WE43 alloy (UNS M18430) [Online]. Available: https://www.azom.com/article.aspx?ArticleID=9279, 2013. (Accessed 7 October 2021).
[33] ASTM International, ASTM standard F3268-18a, in: Standard Guide for in Vitro Degradation Testing of Absorbable Metals, 2018. West Conshohocken, PA.
[34] J. Schindelin, I. Arganda-Carreras, E. Frise, V. Kaynig, M. Longair, T. Pietzsch, S. Preibisch, C. Rueden, S. Saalfeld, B. Schmid, J. Tinevez, D. White, V. Hartenstein, K. Eliceiri, P. Tomancak, A. Cardona, Fiji: an open-source platform for biological-image analysis, Nat. Methods 9 (2012) 676–682.
[35] I. Arganda-Carreras, V. Kaynig, C. Rueden, K. Eliceiri, J. Schindelin, A. Cardona, H. Seung, Trainable Weka Segmentation: a machine learning tool for microscopy pixel classification, Bioinformatics 33 (15) (2017) 2424–2426.
[36] N. Schell, A. King, F. Beckmann, T. Fischer, M. Müller, A. Schreyer, The high energy materials science beamline (HEMS) at PETRA III, Mater. Sci. Forum 772 (2013) 57–61.
[37] M. Basham, J. Filik, M. Wharmby, P. Chang, B. El Kassaby, M. Gerring, J. Aishima, K. Levik, B. Pulford, I. Sikharulidze, D. Sneddon, M. Webber, S. Dhesi, F. Maccherozzi, O. Svensson, S. Brockhauser, G. Naray, A. Ashton, Data analysis WorkbeNch (DAWN), J. Synchrotron Radiat. 22 (2015) 853–858.
[38] W. Nitz, A. Oppelt, W. Renz, C. Manke, M. Lenhart, J. Link, On the heating of linear conductive structures as guide wires and catheters in interventional MRI, J. Magn. Reson. Imag. 13 (1) (2001) 105–114.
[39] P. Nordbeck, F. Fidler, I. Weiss, M. Warmuth, M. Friedrich, P. Ehses, W. Geistert, O. Ritter, P. Jakob, M. Ladd, H. Quick, W. Bauer, Spatial distribution of RF-induced E-fields and implant heating in MRI, Magn. Reson. Med. 60 (2) (2008) 312–319.
[40] R. Willumeit-Römer, The interface between degradable Mg and tissue, Characterization of Biodegradable Medical Materials 71 (4) (2019) 1447–1455.

[41] M. Ascencio, M. Pekguleryuz, S. Omanovic, An investigation of the corrosion mechanisms of WE43 Mg alloy in a modified simulated body fluid solution: the influence of immersion time, Corrosion Sci. 87 (2014) 489–503.
[42] G. Galicia, N. Pebere, B. Tribollet, V. Vivier, Local and global electrochemical impedances applied to the corrosion behaviour of an AZ91 magnesium alloy, Corrosion Sci. 51 (8) (2009) 1789–1794.
[43] N. Mcintyre, C. Chen, Role of impurities on Mg surfaces under ambient exposure conditions, Corrosion Sci. 40 (10) (1998) 1697–1709.
[44] I. Marco, F. Feyerabend, R. Willumeit-Römer, O. Van der Biest, Degradation testing of Mg alloys in Dulbecco's modified eagle medium: influence of medium sterilization, Mater. Sci. Eng. C 62 (2016) 68–78.
[45] B. Zeller-Plumhoff, D. Laipple, H. Slominksa, K. Iskhakova, E. Longo, A. Hermann, S. Flenner, I. Greving, M. Storm, R. Willumeit-Römer, Evaluating the morphology of the degradation layer of pure magnesium via 3D imaging at resolutions below 40 nm, Bioact. Mater. 6 (12) (2021) 4368–4376.
[46] A. Hänzi, P. Gunde, M. Schinhammer, P. Uggowitzer, On the biodegradation performance of an Mg–Y–RE alloy with various surface conditions in simulated body fluid, Acta Biomater. 5 (1) (2009) 162–171.
[47] E. Öcal, Z. Esen, K. Aydinol, A. Dericioglu, Comparison of the short and long-term degradation behaviors of as-cast pure Mg, AZ91 and WE43 alloys, Mater. Chem. Phys. 241 (2020).
[48] D. Liu, Y. Ding, T. Guo, X. Qin, C. Guo, S. Yu, S. Lin, Influence of fine-grain and solid-solution strengthening on mechanical properties and in vitro degradation of WE43 alloy, Biomed. Mater. 9 (2014).
[49] A. Anesi, M. Di Bartolomeo, A. Pellacani, M. Feretti, F. Cavani, R. Salvatori, R. Nocini, C. Palumbo, L. Chiarini, Bone healing evaluation following different osteotomic techniques in animal models: a suitable method for clinical insights, Appl. Sci. 10 (20) (2020) 7165.
[50] MatWeb, LLC, MatWeb: Material Property Data, 1996. -2022. [Online]. Available: https://www.matweb.com/index.aspx. (Accessed 14 July 2022).
[51] M. Capek, J. Eichler, P. Hazdra, Evaluating radiation efficiency from characteristic currents, IET Microw., Antennas Propag. 9 (1) (2015) 10–15.
[52] C. Armenean, E. Perrin, M. Armenean, O. Beuf, F. Pilleul, H. Saint-Jalmes, RF-induced temperature elevation along metallic wires in clinical magnetic resonance imaging: influence of diameter and length, Magn. Reson. Med. 52 (5) (2004) 1200–1206.
[53] S. Seshadri, J. Scott, Enhancing skin-effect using surface roughening and its potential to reduce RF heating from implant leads, in: Electronics New Zealand Conference, 2017.
[54] G. Gold, K. Helmreich, A physical model for skin effect in rough surfaces, in: 7th European Microwave Integrated Circuit Conference, 2012.
[55] A. Horn, J. Reynolds, J. Rautio, Conductor profile effects on the propagation constant of microstrip transmission lines, in: IEEE MTT-S International Microwave Symposium, 2010.
[56] D. Gensler, F. Fidler, P. Ehses, M. Warmuth, R. Reiter, M. Düring, O. Ritter, M. Ladd, H. Quick, P. Jakob, W. Bauer, P. Nordbeck, MR safety: fast T 1 thermometry of the RF-induced heating of medical devices, Magn. Reson. Med. 68 (5) (2012) 1593–1599.
[57] A. Yao, M. Murbach, T. Goren, E. Zastrow, W. Kainz, N. Kuster, Induced radiofrequency fields in patients undergoing MR examinations: insights for risk assessment, Phys. Med. Biol. 66 (2021).
[58] P. Sekar, N. S, V. Desai, Recent progress in in vivo studies and clinical applications of magnesium based biodegradable implants – a review, Journal of Magnesium and Alloys 9 (4) (2021) 1147–1163.